Articles in PresS. J Neurophysiol (June 7, 2017). doi:10.1152/jn.00117.2017

Robotic navigation to sub-cortical neural tissue for intracellular electrophysiology in vivo

WA Stoy[1], I Kolb[1], GL Holst[2], YJ Liew[1], A Pala[1], B Yang[2], ES Boyden[3,4], GB Stanley[1], CR Forest[1,2]

[1] Wallace H. Coulter Department of Biomedical Engineering, Georgia Institute of Technology, Atlanta GA, 30332 USA

[2] George W. Woodruff School of Mechanical Engineering, Georgia Institute of Technology, Atlanta GA, 30332 USA

[3] Media Lab, Massachusetts Institute of Technology, Cambridge, MA

[4] McGovern Institute for Brain Research, Massachusetts Institute of Technology, Cambridge, MA

ABSTRACT

In vivo studies of neurophysiology using the whole-cell patch clamp technique enable exquisite access to both intracellular dynamics and cytosol of cells in the living brain but are underrepresented in deep subcortical nuclei due to fouling of the sensitive electrode tip. We have developed an autonomous method to navigate electrodes around obstacles such as blood vessels, after identifying them as a source of contamination during regional pipette localization (RPL) in vivo. In mice, robotic navigation prevented fouling of the electrode tip, increasing RPL success probability 3 mm below the pial surface to 82% (n=72/88) over traditional, linear localization (25%, n=24/95) and resulted in high quality thalamic whole-cell recordings with average access resistance (32.0 MΩ), and resting membrane potential (-62.9 mV) similar to cortical recordings in isoflurane-anesthetized mice. Whole-cell yield improved from 1% (n=1/95) to 10% (n=9/88) when robotic navigation was used during RPL. This method opens the door to whole-cell studies in deep subcortical nuclei, including multimodal cell typing and studies of long range circuits.

NEW AND NOTEWORTHY

This work represents an automated method for accessing subcortical neural tissue for intracellular electrophysiology in vivo. We have implemented a novel algorithm to detect obstructions during regional pipette localization and move around them while minimizing lateral displacement within brain tissue. This approach leverages computer control of pressure, manipulator position, and impedance measurements to create a closed-loop

platform for pipette navigation in vivo. This technique enables whole-cell patching studies to be performed throughout the living brain.

INTRODUCTION

In vivo patch clamp recording is one of the most important and versatile techniques in neuroscience. Whole-cell recordings have enabled stable investigation of subthreshold activity to identify cell types and circuits in the intact brain. This technique is also uniquely positioned to enable concurrent measurements of intrinsic and sensory evoked electrophysiology in either voltage- or current-clamp modes (Harvey, Collman, Dombeck, & Tank, 2009) (Constantinople & Bruno, 2013), morphology (Margrie, Brecht, & Sakmann, 2002), and the genetic profile of single neurons (Cadwell et al., 2016), as well as the ability to introduce foreign genetic material into the cell ((Rancz et al., 2011), (Vélez-Fort et al., 2014)). There is growing interest in multimodal cell type classification (electrophysiological, morphological, and/or genetic, etc.) throughout the brain, a major goal of the BRAIN Initiative (Bargmann, Newsome, & Anderson, 2014). Though recently developed genetic voltage indicators have been used with some success to measure activity both from individual neurons and populations (Lin & Schnitzer, 2016), the heterogeneous tissue of the brain acts as a scattering medium, limiting recordings to superficial cortical layers in the mammalian brain. Sharp intracellular recording techniques similarly have sub-threshold resolution, but suffer from short recording times (Fee, 2000) and are unsuitable for voltage-clamp recordings due to high electrode impedance.

While whole-cell patch clamping is the gold standard for in vivo electrophysiology, it requires skill to perform and has thus been more extensively used for in vitro experiments. Recent efforts to automate it have been productive, yet sub-cortical recording with whole-cell patch clamping remains a low yield endeavor. Published papers are scant ((Margrie et al., 2002), (Brecht & Sakmann, 2002), (Groh et al., 2014)), but whole-cell recordings in deep subcortical nuclei are difficult to obtain and are known to suffer from increased access resistance (Margrie et al., 2002). In a literature review of the 60 most cited papers that reported low access resistance, blind, whole-cell recordings *in vivo*, only 5% of all 2350 recorded cells were recorded at depths exceeding 3 mm from the pial surface in rodents. Several other studies have demonstrated recordings in the cat thalamus in vivo (several centimeters below the pial surface), but report high access resistance of the electrodes (X. Wang, Vaingankar, Sanchez, Sommer, & Hirsch, 2011; X. Wang et al., 2007).

To investigate these subcortical nuclei in vivo, researchers have used extracellular, juxtasomal, cell-attached, or sharp intracellular recordings ((Q. Wang, Webber, & Stanley, 2010a), (Yu, Xiong, Chan, & He, 2004b),(Petersen et al., 2008),(Higley & Contreras, 2007),(Friedberg, Lee, & Ebner, 2004),(Polack & Charpier, 2006),(Yu, Xiong, Chan, & He, 2004a)), indicating that deep whole-cell recordings, while valuable and desirable, are exceedingly difficult to obtain. In order to enable this important technique to be used throughout the brain, we identify a need to improve both the yield and quality of deep whole-cell recordings.

It is well known that a pipette must be clean, with a good tip geometry, to enable formation of a gigaseal with a target cell (Neher, 1995). Since deep recording requires

traversing through several millimeters or centimeters of heterogeneous tissue (e.g., blood vessels, glial cells, membranes) to reach a region of interest during regional pipette localization (RPL), the pipette invariably encounters, and is clogged by debris from this tissue. Effort to date to mitigate this problem have had limited success. In their 2002 study, Margrie et al. suggested that increasing pipette pressure or advancing the pipette through a guide tube may reduce access resistance (or equivalently, increase quality) (Margrie et al., 2002). However, Brecht and Sakmann subsequently noted that neither higher pressures nor a guide tube reduced the access resistance of thalamic recordings (Brecht & Sakmann, 2002).

We set out to investigate the relationship between this troublesome first stage of patch clamping, regional pipette localization, and high access resistance, low yield whole-cell experiments. By attempting whole-cell trials in the mouse thalamus, a deep brain structure of wide interest ((Kelly et al., 2014), (Llinás & Steriade, 2006), (Sherman, 2005)), we observed that transient high amplitude fluctuations in resistance that occur during regional pipette localization are often followed by residual, permanent increases in pipette tip resistance, preventing successful whole-cell recordings, and that these obstructions could be avoided with a series of small lateral movements, confirming previous observations by Lee et al. 2014 (D. Lee, Shtengel, Osborne, & Lee, 2014). By visualizing this process using slices of brain tissue on a microscope, we show that pipette penetration of blood vessels and the residue left on pipette tips is the likely cause these resistance changes, along with meninges (dura, pia, and hippocampal meninges). Lateral steps enabled navigation around blood vessels and other obstacles

without a residual increase in resistance and meninges were penetrated with short, rapid plunges with the pipette. We developed an efficient algorithm for laterally moving around obstructing blood vessels during regional pipette localization in vivo and compared its effectiveness to linear localization. We found that whole-cell trials performed 3 mm deep could be localized with the same yield as we had previously demonstrated in the cortex (up to 1 mm) with direct linear localization and in addition, had comparable access resistances to whole-cell recordings performed previously in the cortex.

MATERIALS AND METHODS

Acute in vivo and in vitro preparation

All experiments were performed in accordance with the Georgia Tech Institutional Animal Care and Use Committee (IACUC) guidelines. For in vivo preparation, all mice (n=19) were prepared for acute experimentation as we have done previously (Kodandaramaiah, Franzesi, Chow, Boyden, & Forest, 2012). Briefly, young male C57BL/6 mice (p35–p49) were anesthetized with isoflurane and headfixed to a titanium headplate with C&B-Metabond dental cement (Parkell, Edgewood, NY). Craniotomies (1 mm diameter) and duratomies were performed above the Ventral Posteromedial nucleus (VPM) of the thalamus (1.75 mm Rostral, 1.75 mm Lateral, 3 mm below the pial surface) using stereotaxic coordinates from the Paxinos and Franklin mouse brain atlas (Paxinos 2012).

For in vitro preparation, acute brain slices of mouse visual area VI were prepared from male C57BL/6 adult mice (aged P30-P60) using the protective recovery method described in detail elsewhere (Wu 吴秋雨 et al., 2016).

Pipette fabrication

Long taper patch pipettes (e.g., 7 mm) were pulled using fire-polished borosilicate glass (BF150-86-10HP, Sutter Instrument, Novato, California) on a P-1000 electrode puller with a 4.5 mm wide box filament (Sutter Instrument). The long taper is achieved with an initial high-velocity step (heat = Ramp + 10, velocity = 40), with subsequent steps used to develop the taper to ~1 µm (3-4 pulls of heat = Ramp – 10, velocity = 20).

Electrophysiology

Whole-cell patch clamping was performed as described previously (Kodandaramaiah 2016). In brief, an Autopatch 1500 (Neuromatic Devices, Atlanta GA) was used to provide computer-controlled pressure and measure resistance for both in vitro and in vivo experiments. Both in vitro and in vivo experiments used Multiclamp 700B amplifiers (Molecular Devices, Sunnyvale, CA) and signals were digitized at 20kHz using National Instruments DAQs (in vivo DAQ: cDAQ-9174 and NI 9215, in vitro DAQ: NI USB-6221, National Instruments, Austin, TX) and recorded in PClamp 10 (Molecular Devices). A Slicescope Pro 1000 (Scientifica, Essex, UK) was used to perform *in vitro* recordings and an MP-285 micromanipulator (Sutter Instrument) with PT1-Z8 Motorized Translation stage (Thorlabs, Newton, New Jersey) was used for positioning the electrode for in vivo patch clamping.

Resistance measurements were performed throughout pipette translation, rather than only before and after translation as in our prior work ((Kodandaramaiah et al., 2012), (Kodandaramaiah et al., 2016)). During pipette translation, starting from ACSF on the surface of the tissue, resistance was recorded by applying a 20 mV amplitude, 128 Hz square wave (50% duty cycle) to the pipette, and calculating the resistance using Ohm's law. The resistance was computed as a moving average of four measurements (low pass filter with four sample rectangular window). Thus, filtered resistances were saved to an array, called the resistance array.

Blood vessel penetration

In addition to mapping a blood vessel in neural tissue using SCIM, we measured the resistance changes encountered as the pipette was translated *through* a blood vessel in vitro. The pipette was filled with ACSF and pressured to high positive pressure (1000 mbar) to replicate typical parameters for in vivo pipette localization (Kodandaramaiah et al., 2016). For this penetration experiment, the pipette was positioned above a blood vessel visually, at 35° relative to the image plane. The pipette was manually lowered until the tip resistance increased by 12.5% above initial pipette resistance, and then retracted 15 μm to a starting position. Resistance was recorded while the pipette was manually advanced for 200 μm as described above. Images were captured at relative depths indicated using the optical system (See Fig. 2B).

Scanning ion conductance microscopy in vitro (SCIM)

We mapped blood vessels in neural tissue (in vitro) by performing scanning ion conductance microscopy (Sánchez et al., 2008). The pipette was filled with ACSF and pressurized to low positive pressure (30 mbar). First, the pipette was centered above a blood vessel of interest and visualized using differential interference contrast (DIC) optical system (Olympus, Center Valley, PA). The pipette was manually lowered until the tip resistance increased by 12.5% above initial pipette resistance. The pipette was then retracted 15 μm and moved laterally to a new, random "grid position." At this new position, the pipette was then moved down 15 μm and the tip resistance was measured again. This process was performed repeatedly until all grid positions were measured. A grid is defined as a square 20 μm x 20 μm comprising 100 "grid positions" with 2 μm pitch, centered on the initial pipette axial position. The resulting map of resistances as a function of lateral pipette position (at constant depth) was linearly interpolated to 1 μm pitch for visualization and displayed in MATLAB (Natick, MA) as a surface plot (See Fig. 2C).

Regional pipette localization (RPL) in vivo

Regional pipette localization (Kodandaramaiah et al., 2012) refers to the act of lowering a pipette into neural tissue to a desired region of interest (e.g., thalamus) under high positive pressure. In our experiments, we performed regional pipette localization using two different methods: an uninterrupted, direct, linear trajectory as we have previously described (Kodandaramaiah et al., 2012) and a novel robotic navigation method to avoid obstructions. The method of localization was randomly selected prior to each trial. A maximum of 10 electrode penetrations were performed per experimental preparation.

Pipettes were initially placed on the brain surface under stereoscopic guidance in a region free of large blood vessels.

a. RPL using linear trajectory

Linear regional pipette localization has previously been utilized by us (Kodandaramaiah et al., 2012) and others (Desai, Siegel, Taylor, Chitwood, & Johnston, 2015) for whole-cell electrophysiology in vivo. We used similar parameters; briefly, we applied high positive pressure (1000 mbar) and translated the pipette at a rate of 500 μm/s. Resistance was recorded during localization as described above, so the resistance array could be displayed and analyzed, at a pitch of 500 μm/s / 128 Hz = 3.9 μm/sample.

b. RPL using robotic navigation

For RPL using robotic navigation, high positive pressure (800 mbar) was applied and the pipette was translated at a rate of 200 μm/s, unless otherwise stated. Resistance was recorded during localization as described above. At the square wave frequency of 128 Hz, resistance array measurements were spaced 1.6 μm apart. The pipette was inserted along its initial axis, z, at x,y = (0,0) and moved in x, y, and z to navigate around obstacles.

As shown in Fig. 3, if an obstruction was detected during localization, motion was halted at depth $z_{obstruction}$, with a pipette resistance of $R_{obstruction}$ (note Fig. 3b1,c). An obstruction detection was defined as follows: pipette resistance increase of at least of 12.5% above baseline resistance. Baseline resistance, $R_{baseline}$, was computed as the minimum resistance of the previous 800 μm (512 samples from the resistance array, 4 sec). With an initial pipette resistance of 4-7 MΩ, 12.5% increase resulted in a minimum $R_{obstruction}$ of 4.5-7.9 MΩ.

After halting the motion of the pipette upon obstruction detection, the pipette is moved in a series of steps in an attempt to navigate around the obstruction. First, the pipette is retracted along the pipette axis (z) by a distance z_{dodge} (See Fig. 3b2,c). The distance z_{dodge} is located relative to $z_{obstruction}$ within the previous 50 μm (32 samples) at which a minimum pipette resistance, R_{dodge}, was recorded. At depth z_{dodge}, the pipette is moved laterally to dodge, or navigate around, the obstacle that was encountered (See Fig. 3b3,c). Lateral movements, centered on the initial pipette axis are calculated to form a spiral (See Fig. 3c), as follows:

$$m(n) = n\Delta r \cos(n\Delta\theta - \pi/4)\,\boldsymbol{i} + n\Delta r \sin(n\Delta\theta - \pi/4)\,\boldsymbol{j}$$

Where Δr = 5 μm, $\Delta\theta = \pi/4$, and n is the step index {1, 2, 3, ...}. Each step, n, yields a lateral movement vector, m, along which the pipette is moved. The pipette is then lowered back to $z_{obstruction}$ (See Fig. 3b4,c). At $z_{obstruction}$, the resistance is measured again, termed R_n. If $R_n - R_{dodge} \geq 200$ kΩ, the obstacle is still in the proximity of the pipette

tip and has not been avoided. The pipette is then retracted to z_{dodge}, the step index n is incremented, and another later movement occurs. This is repeated until R_n-R_{dodge} < 200 kΩ or until n=10, resulting in a maximum lateral distance of 50μm.

If R_n-R_{dodge} < 200 kΩ, the obstacle has been successful avoided. The pipette is advanced 30 μm beyond z_{dodge} to ensure the obstacle has been passed (See Fig. 3b5,c)., and then the pipette is moved laterally in a straight line from $x,y = (mi(n), mj(n))$ to return to the initial pipette axis, $x,y = (0,0)$ (See Fig. 3b6,c).

Alternatively, if n=10 and R_n-R_{dodge} ≥ 200 kΩ, the obstacle was not avoided. In this case, a pulse of high positive pressure (1000 mbar, 1 sec) is applied while the pipette is advanced 100 microns at 200 μm/s to attempt to dislodge the obstruction from the tip of the pipette. The pipette is then moved laterally in a straight line to return to the initial pipette axis, $x,y = (0,0)$ (See Fig. 3c).

Localization is continued until the region of interest is reached and the pipette resistance is less than 200 kΩ above the baseline resistance, R_b. If the obstruction is not cleared before the end of the region of interest, pipette localization is halted and the pipette is retracted to the surface and replaced.

Following successful regional pipette localization, the software compensates for pipette capacitance, which is expected to change due to the depth of the recordings discussed here.

RESULTS

RPL using linear trajectory

We have previously developed an automated patch clamping system, the Autopatcher, and deployed it in the cortex and hippocampus. The results for regional pipette localization, and yield are shown in Fig. 1, top row, for depths less than 1 mm, reproduced from Kodandaramaiah et al. 2012.

To explore the feasibility of using the Autopatcher for whole-cell recording in deep subcortical nuclei we targeted the ventral posteromedial (VPM) nucleus and surrounding nuclei of the thalamus. The resulting yield of whole-cell patching was far below what we observed in our previous cortical patching efforts (See Fig. 1, top and middle rows). In 95 trials, one successful whole-cell recording was achieved. Further, in 75% of trials (71/95), the pipette reached a depth of 3 mm with a tip resistance above the threshold for removal and replacement. Thus 75% of trials were aborted without attempting gigaseal formation.

To understand what was occurring during linear localization, we modified the Autopatcher so that, as described in the Methods, resistance measurement was performed throughout pipette translation, rather than only before and after translation as in our prior work. Consequentially, during linear localization multiple high amplitude

fluctuations of the resistance were revealed, occasionally greater than 25 MΩ (Fig. 4 a,b). As the pipette advanced, resistance would often return near, but not exactly back to baseline, indicating that the event was transient. Final pipette resistance (at the depth of regional pipette localization) was on average 730 kΩ greater than the initial resistance measured above the pial surface (Fig. 4e). High amplitude fluctuations were observed in 91% of linear localization trials (n=86/95) (Fig. 4a).

Observations of obstacles

To understand the nature of these high amplitude resistance fluctuations, we investigated them in vitro where we could visualize the interaction of the pipette tip with the neural tissue under a microscope. After applying the requisite high positive pressure (1000 mbar) to a patch pipette, we advanced its tip through the tissue. We noted that the high positive pressure easily displaced neurons and glia, but some blood vessels remained in the path of the pipette. Shown in Fig. 2a, as the pipette encountered one of these blood vessels during manual, axial translation at approximately 15 μm/sec, the pipette resistance was measured at 10 Hz. The pipette resistance, initially 4.3 MΩ, increased to 26 MΩ within 35 μm as the pipette deformed the blood vessel (Fig. 2b). The resistance then quickly decreased as the pipette pierced and passed through the blood vessel. However, a residual blockage was noted, causing an increase in pipette resistance of 3.7 MΩ that persisted until the end of the tissue slice was reached (approximately 200 μm). The resistance signature of an obstruction in vitro appears qualitatively similar to resistance fluctuations encountered in vivo (Compare Fig. 2a and

Fig. 4b)—a rapid increase in resistance, followed by a rapid decrease, resulting in a residual resistance offset.

The previous result showed the uniaxial *(z)* signatures of a blood vessel encountered with a pipette. We also mapped blood vessels in neural tissue laterally *(x,y)* by performing scanning ion conductance microscopy. As shown in Fig. 2c-e, pipette resistance increases were observed over a region that overlapped with the microscopy image of the blood vessel. Concomitantly, regions of tissue adjacent to the blood vessel, populated by neural cells and glia, showed only negligible resistance increases. Additionally, without impaling the blood vessel, no residual increase in resistance was noted even after 100 consecutive resistance measurements. Thus, we gained confidence that a blood vessel was the predominant obstacle to pipette insertion in neural tissue and that it could be avoided by moving the pipette laterally even after initial contact if the vessel was not impaled.

Selection of Navigation Algorithm Parameters

We used SCIM to further optimize the parameters for encountering, and navigating around obstacles. We set a threshold for obstacle encounters of 12.5% (approximately 500 kΩ); this is greater than the amplitude of baseline resistance variation during localization (100 kΩ) but much less than observed during blood vessel impalement (See Fig. 2a).

To determine the axial retraction distance necessary to attempt to dodge an obstacle, z_{dodge}, we first noted that the pipette can drag cells and blood vessels if it is positioned too close to an obstacle. We moved the pipette above a blood vessel and determined the minimum axial retraction distance required to allow a pipette to move laterally without dragging an obstruction to be 15 μm (data not shown). We set a retraction distance of up to z=50 μm in vivo to ensure that the pipette was safely away from the obstacle before lateral motion, given that the in vivo environment is less predictable than in vitro.

We next attempted to optimize the axial advancement distance necessary to bypass an obstacle after lateral movement. Others have performed a rigorous study of blood vessels in the mouse brain, showing sizes of 10-60 μm ((Santisakultarm et al., 2012), Fig. 2c). From their data, we compute a mean blood vessel diameter of 28.1 ± 1.9 μm. In our observations, capillaries 15 μm diameter and smaller were easily displaced under high positive pressure. We set a distance of 30 μm to advance the pipette beyond the blood vessel location ($z_{obstruction}$) to ensure the obstacle had been passed.

Whereas we used 1000 mbar for RPL during linear localization, we chose a lower pressure (800 mbar) for pipette insertion during robotic navigation to reduce the volume of ejected intracellular solution during the longer time needed to perform RPL.

To minimize damage to the tissue in vivo, we designed the vessel avoidance algorithm to make the smallest lateral and radial movements possible. Radial movement was

356 defined as the distance between the pipette position (x_n,y_n) and the original pipette
357 location at $x,y = (0,0)$. Lateral distance traveled was defined as the sum of the distances
358 traveled between each point. Movements were made in small increments to minimize
359 radial distance, r, traveled. Additionally, because the orientation of the blood vessel's
360 major axis with respect to manipulator's x and y axes is unknown, we incremented the
361 angle, θ with each step resulting in a spiral search pattern. Similar search patterns have
362 been shown to minimize path length when searching for a line in a 2D plane, analogous
363 to finding the edge of a blood vessel in a plane (Finch 2016).
364
365 *RPL using robotic navigation*
366 Using robotic navigation algorithm to avoid obstructions during regional pipette
367 localization greatly improved the yield of successfully localized pipettes. In 88 trials,
368 82% of pipettes were localized successfully to a depth of 3000 μm when the dodging
369 algorithm was active (when compared to linear localization, n=95, p=7.8448e-15,
370 Fisher's exact test). This high yield for RPL using robotic navigation for the thalamus is
371 comparable to rates achieved with RPL using linear trajectories in the cortex.
372
373 In addition, the final resistance increase (170 kΩ, n=88) was significantly lower than
374 when the pipette was localized without the algorithm (730 kΩ, n=95, p=0.0142,
375 Wilcoxon rank sum test) (See Fig. 4de). During robotic navigation, obstructions were
376 encountered in 95% of trials, and on average the dodging algorithm attempted to avoid
377 6.7 obstructions during each localization (See Fig. 4c). At a depth of 3000 μm,
378 obstructions were therefore encountered every 3000/6.7=445 μm on average. Each

obstruction that was successfully avoided in n=3.5 steps, resulting in a radial distance of 17.5 μm on average. Regional pipette localization under algorithmic guidance was completed in an average of 75 ± 23 sec, significantly longer than 6 sec (3 mm at 500 μm/s) using the traditional localization method, due to the increased time to avoid obstacles and the lower localization speed. Advantageously, this slow localization may allow tissue to relax before attempting to patch.

The number of robotic navigation events did not have a significant effect on the success of gigasealing. Trials that resulted in a gigaseal (n=17) underwent 3.65 navigation events on average, while trials that failed to result in a gigaseal (n=71) underwent 7.24 navigation events on average (p=0.961 Wilcoxon rank sum test). Additionally, the maximum resistance increase experienced by pipettes during localization did not have an effect on the success of gigasealing. Trials that resulted in a gigaseal (n=17) had an average maximum resistance during localization of 4.9 MOhms, while trials that failed to result in a gigaseal (n=71) had an average maximum resistance during localization of 6.1 MOhms (p=0.19, Wilcoxon rank sum test).

Vertical descent to the thalamus requires penetration of the ventricular meninges, large, relatively planar membranes that cannot be avoided using the algorithm described here. The meninges were routinely detected at approximately 2.5 mm from the pial surface (See Fig. 4h). The meninges were penetrated using, on average, 2.3 successive dodge attempts (each resulting in a rapid 100 μm advancement of the pipette).

The yield of whole-cell recordings in thalamus improved when regional pipette localization was performed using robotic navigation. In trials where whole-cell recordings were attempted following RPL with robotic navigation, 10% of trials (n=9/88) resulted in successful whole-cell recordings. In trials performed using RPL with linear localization, 1% of trials (n=1/95) resulted in whole-cell recordings (p=0.0076, Fisher's exact test).

Whole-cell recordings performed in the thalamus with robotic navigation were of comparable quality to those previously performed in the cortex using linear localization (See Fig. 5, (Kodandaramaiah et al., 2012), (Margrie et al., 2002)). Our thalamic recordings had similar access resistances (32.0 $\pm$ 4.1 MΩ) to cortical recordings reported by Margrie et al. 2002 as well as our prior work, all in the range of 10-50 MΩ ((Margrie et al., 2002), (Kodandaramaiah et al., 2012)). Similarly, our thalamic recordings had holding currents (-50.8 $\pm$ 8.9 pA) at -65 mV holding voltage and resting membrane potentials (-62.9 $\pm$ 2.0 mV) that were not significantly different from our previous cortical work, respectively, -23.5 $\pm$ 12.9 pA (p=0.1982, Wilcoxon rank-sum test) and -61.54 $\pm$ 1.05 mV (p=0.1148, Wilcoxon rank-sum test).

Recorded neurons had electrophysiological properties consistent with ventrobasal thalamic nucleus neurons (VB), consisting of the ventral posteromedial nucleus (VPM) and the ventral posterolateral nucleus (VPL). In response to hyperpolarizing current injection, sag potentials were observed (hyperpolarization induced depolarization, indicative of H currents, I_H (Kuisle et al., 2006; Leist et al., 2016), see Fig. 5b). Following

425 release of hyperpolarizing currents, burst firing was observed indicative of T-type
426 calcium channel activity, often followed by after (spike) depolarization (Kuisle et al.,
427 2006; X. Wang et al., 2010b) (see Fig. 5c arrow).
428
429 Comparison of whole-cell recordings in the thalamus with robotic navigation to those
430 previously reported in the thalamus using linear localization is difficult. There are few
431 reports of successful whole-cell thalamic recordings ((Margrie et al., 2002), (Mease,
432 Sumser, Sakmann, & Groh, 2016), (Oberlaender et al., 2012a), (Brecht & Sakmann,
433 2002)) and the quality metrics are not reported consistently. However, Margrie et al
434 2002 reports that, “Despite the thalamic recordings being carried out on a younger
435 sample of animals the access resistance was consistently greater than that observed for
436 more superficial recordings.” In addition to numerous conversations with other labs
437 performing whole-cell recordings in vivo (personal communication), we assume that the
438 scarcity of published whole-cell recordings far below the cortex in vivo suggest that they
439 are very difficult to achieve. In our hands, the single cell that was recorded using linear
440 localization during RPL was of lower quality with an access resistance of 72 MΩ, resting
441 membrane potential of -45 mV, and holding current of -150 pA.
442
443 **DISCUSSION**
444
445 Here, we describe a method to robotically navigate whole-cell patch pipettes through
446 neural tissue in vivo in a way that significantly reduces clogging of the tips that occurs
447 commonly when blood vessels are pierced. Pipettes localized without robotic navigation

448 frequently encounter (91% of the trials) and impale obstructions during localization, as
449 others have previously noted ((Margrie et al., 2002), (Brecht & Sakmann, 2002), (A. K.
450 Lee, Epsztein, & Brecht, 2009)). This is tolerable for cortical recordings, but as we have
451 shown obstacles are encountered on average every 370 μm and therefore make deep,
452 sub-cortical recordings in vivo impractically low yield and quality.
453
454 Previous studies have noted the existence and detrimental effect of permanent
455 resistance increases during RPL ((Margrie et al., 2002), (D. Lee et al., 2014)),
456 speculating that electrode penetration of the vasculature was the cause (D. Lee et al.,
457 2014). We have shown, through in vitro studies, that these obstructions are very likely
458 caused by encounters with blood vessels larger than 15 μm. Following these
459 encounters, vascular membrane residue adhering to the pipette tip obstructs the tip and
460 increases residual resistance. An efficient spiral navigation algorithm to find the edge of
461 the blood vessel with minimal tissue displacement (17.5 μm on average) enables high
462 yield regional pipette localization.
463
464 Robotic navigation enables one to localize pipettes in deep structures (e.g., mouse
465 thalamus at 3 mm) with yields similar to those reported in the cortex using linear
466 localization. Pipettes were successfully localized with robotic navigation to a depth of 3
467 mm below the pial surface in 82% of trials (n=72/88), comparable to linear localization in
468 the cortex from our previous study (81%, n=128/158, p=1, Fisher's exact test)
469 (Kodandaramaiah et al., 2012).
470

For whole-cell recording yield, there are large ranges of reported yields that make comparison more challenging. Whole-cell yield for blind in-vivo patching has been reported between 20-50% ((Margrie et al., 2002), (A. K. Lee et al., 2009)), while the yield for two photon targeted patching in mice *in vivo* is between 10-20% (Margrie et al., 2003). For blind, automated whole-cell recording in the mouse cortex, we have previously reported a yield of 31% (Kodandaramaiah et al., 2012). Others have reported yields of 17% (Desai et al., 2015) in mice using similar automation. Our yield of 10% in the mouse thalamus makes recording there practical, although somewhat lower yield than cortical whole-cell recording. Additionally, we believe that all subcortical nuclei are now accessible using this method, as electrodes inserted to the VPM must traverse white and gray matter. However, there may still be regions of the brain that may be difficult to access due to their proximity to the ventricles. In this work, we did not address the penetration of the thick ventricular membranes as such membranes are likely impossible to navigate around, and would release CSF into the brain if punctured. Penetration of such membranes remains a problem for maintaining the cleanliness of the electrode, but might be mitigated with the application of a reversible, protective coating (Singh, Zhu, & He, 2004). The advent of further automation strategies such as pipette cleaning (Kolb et al., 2016) may further improve the throughput of these experiments.

The whole-cell recording yield is the product of the yield of the four stages of the patch algorithm (See Fig. 1). We note a decrease in gigaseal formation yield with deep patching that is irrespective of localization method, linear or robotic. We have observed

higher amplitude heartbeat modulation during the preceding stage, neuron hunting, for the thalamus relative to the cortex, which may indicate greater mechanical disturbances at these depths affecting gigaseal yield. Identifying and overcoming gigaseal yield issues would further advance deep whole-cell patch clamping efforts and motivate further investigation.

One possible opportunity for improved gigaseal yield is to use the lateral steps performed during SCIM to map target cells prior to gigaseal attempt to optimize the tip placement with respect to the soma, both in vivo and in vitro. Blind in vitro whole-cell recordings suffer from low yield (generally 50-80% in vitro, (Blanton, Loturco, & Kriegstein, 1989)) when compared to image guided in vitro studies (> 80%) (Stuart, Dodt, & Sakmann, 1993). Notably, in vitro resistance measurements alone are not sufficient to identify cell membrane dimpling and cell shape, visual identifiers commonly used to align pipettes with target cells for successful gigaseals (Desai et al., 2015). Further, local membrane stiffness, a potential proxy for membrane dimpling, can be estimated by modulating pressure and measuring the difference in tip resistance (Sánchez et al., 2008). The combination of pressure modulation and scanning ion conductance microscopy may improve pipette placement on cell membranes and thereby increase the yield of single cell experiments in vivo and in vitro.

Leakage of biocytin-containing intracellular solution into the surrounding tissue during RPL may cause background and off-target staining. Intracellular solution in the extracellular space is also undesirable due to the osmotic pressure it places on

neurons. This problem may be compounded by the extended time (75 ± 23 sec vs 6 sec) spent navigating the pipette through tissue under high positive pressure towards the region of interest. Intracellular solution leakage could be reduced by decreasing the positive pressure during RPL. We hypothesize that a lower pipette pressure during RPL will lead to an increase in obstacle detections as less debris, cells, and blood vessels are displaced by the pipette pressure, however the optimal pipette pressure was not investigated in this work. Alternatively, cellular contrasts that are not taken up by cells from the extracellular space, such as DNA plasmids, may reduce off-target labeling (Vélez-Fort et al., 2014).

The average number of navigation events (detected obstacles) for trials that eventually successfully formed a gigaseal (3.65) was lower than for trials that eventually failed to form a gigaseal (7.24). While we found that this difference was not statistically significant, we believe the difference in the means is due to the skew of the navigation event distribution. That is, several failed trials resulted from RPL where successive obstacle detections were triggered throughout their descent, either because they were clogged from internal debris or because accrued debris was not successfully dislodged during the navigation events. Although the pipette resistance ultimately returned to baseline in these trials, we suspect that the tip of the pipette may have become contaminated, but not measurably clogged. Trials with high numbers of successive obstacle detections may indicate unsuccessful navigation and the overall success rate may improve by rejecting these trials.

Intracellular recording has remained as the gold standard electrophysiology technique because of its high quality, mechanical stability, and resolution. Margrie et al. hypothesized that pipette contamination results in higher access resistances, and thus lower quality thalamic recordings. Previous efforts to reduce the access resistance of recordings performed deep in the brain using higher pressures in the pipette or a guide tube have not been successful (Brecht & Sakmann, 2002). Here, we demonstrate that robotic navigation around blood vessels in vivo results not only in higher yield than with linear localization but also higher-quality recordings. Critically, we demonstrate that robotic navigation during regional pipette localization produces whole-cell recordings 3 mm below the pial surface with access resistances similar to those measured from cells in the cortex ((Kodandaramaiah et al., 2012), (Margrie et al., 2002)). Other factors may contribute to differences in yield and access resistance, namely pipette shape and tip geometry, but these parameters are rarely reported or quantified, making comparison difficult. Other parameters were also comparable to previous recordings in cortex, including holding current (voltage clamp, used to keep the cell at -65mV) and resting membrane potential (Kodandaramaiah et al., 2012). Thus, we are confident that in vivo whole-cell recording quality is improved from previous efforts to perform whole-cell recordings in the thalamus and are of equivalent quality to recordings in the cortex.

There are very few published studies that show *in vivo* whole-cell recordings at depths 3 mm or greater. In fact, to our knowledge, only 7 such studies have been published to date ((Mease et al., 2016),(Groh et al., 2014),(Oberlaender et al., 2012a),(Oberlaender, Ramirez, & Bruno, 2012b),(Kuo & Wu, 2012),(Brecht & Sakmann, 2002),(Margrie et al.,

2002)). In contrast, *in vitro* whole-cell recordings in deep subcortical nuclei are abundant ((Kase, Inoue, & Imoto, 2012),(Neuhoff, Neu, Liss, & Roeper, 2002),(Benavides et al., 2007),(Guo et al., 2012),(Hu, Nasif, Zhang, & Xu, 2008),(Sosulina, Graebenitz, & Pape, 2010),(Porcello, Ho, Joho, & Huguenard, 2002)). This indicates that there is interest in performing high-yield subcortical whole-cell recordings in vivo, while recording depth is an impediment for whole-cell studies in these nuclei. Additionally, the whole-cell patch clamp technique is uniquely positioned to investigate the structure-function-gene relationship (Cadwell et al., 2016). This study opens the door for whole-cell electrophysiology coupled with genetic or morphological profiling throughout the entire brain, which is the focus of worldwide effort ((Oberlaender et al., 2012a), (Arkhipov et al., 2016), (Vélez-Fort et al., 2014), (Cadwell et al., 2016)) and a major goal of the Brain Research through Advancing Innovative Neurotechnologies (BRAIN) Initiative (Bargmann et al., 2014).

FIGURES

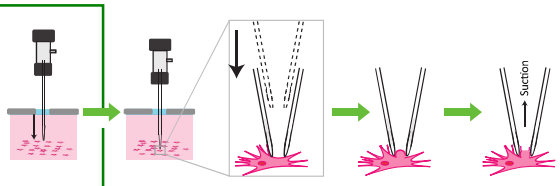

Region	Depth	RPL Method	Regional Pipette Localization (RPL)	Neuron Hunting	Gigaseal Formation	Break In	Total Yield
Cortex	≤ 1 mm	Linear	81%	93%	51%	82%	31%
Thalamus	≥ 3 mm	Linear	25%	88%	10%	50%	1%
		n=	24/95	21/24	2/21	1/2	1/95
Thalamus	≥ 3 mm	Robotic	82%	89%	26%	53%	10%
		n=	72/88	64/72	17/64	9/17	9/88

Figure 1: Increased yield of RPL during whole-cell patching in vivo with robotic navigation. In vivo whole-cell recording is a serial process consisting of Regional Pipette localization, Neuron Hunting, Gigaseal Formation, and Break-In. Whole-cell recording yield (Total) is a linear product of previous success rates. During traditional, linear localization, cortical (top row) and thalamic pipettes (middle row) are clogged in 1/5 insertions and 3/4 insertions respectively, preventing further steps. Gray box indicates procedures presented in this study. The percentage of pipettes that successfully performed regional pipette localization increased from 25% to 82% and total whole-cell yield increased from 1% to 10% when robotic navigation was performed. (top row data reproduced from (Kodandaramaiah et al., 2012))

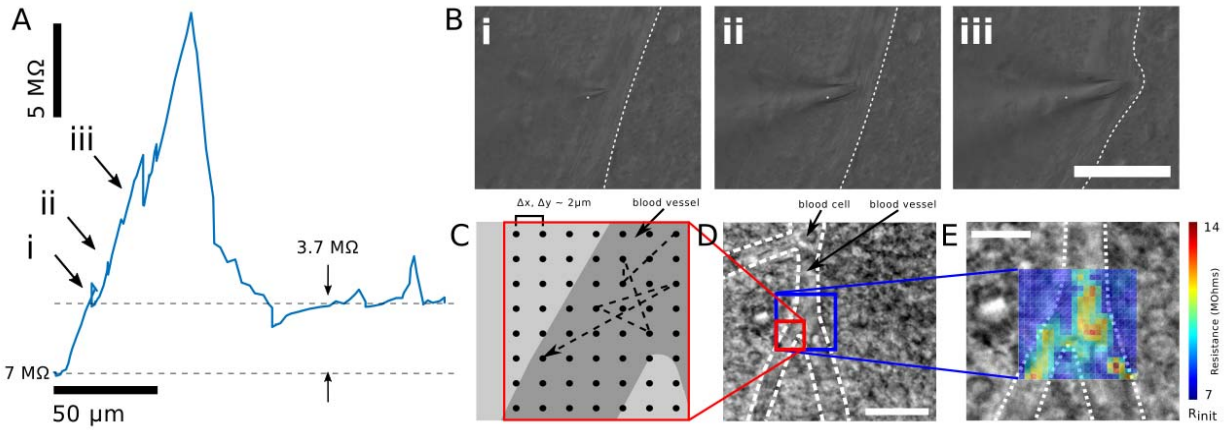

Figure 2: Lateral navigation around obstructions prevents persistent pipette resistance increase caused by penetration of blood vessels in vitro. A) Resistance trace as a function of distance as a pipette pierces a blood vessel under high positive pressure. A residual resistance increase of 3.7 MΩ remains after the vessel is punctured. B) IR DIC images showing the pipette encountering and deforming the blood vessel (scale bar, 50 µm). C) Schematic of Scanning Ion Conductance Microscopy (SCIM) mapping of a blood vessel proceeds from a central point. Samples are collected randomly from a grid area 20 x 20 µm at 2 µm resolution D) The entire blood vessel and surrounding milieu is shown under IR DIC (scale bar, 20 µm) E) Resistances mapped as a function of grid position, clearly showing increased resistance when the pipette is above the blood vessel (scale bar, 10 µm, 2x interpolation)

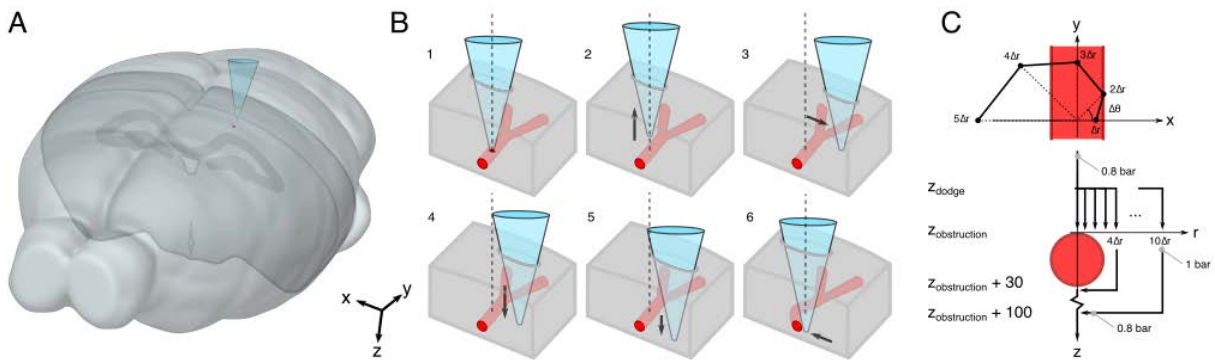

Figure 3: Robotic navigation algorithm for avoiding blood vessels during regional pipette localization in vivo. A) Schematic showing vascular avoidance preparation. Brain outline from the Allen Institute's Mouse Brain Explorer program. B) Visual algorithm of vascular avoidance [1] Obstruction (here, a blood vessel) is detected by an increase in pipette resistance. [2] The pipette is retracted to z_{dodge}, [3] moved laterally, and [4] advanced to the original $z_{obstruction}$. If the difference in resistance at $z_{obstruction}$ and the resistance at z_{dodge} is < 200 kΩ, [5] the pipette is advanced through $z_{obstruction}$ and [6] the pipette is moved back to the original x and y axis. C) The pipette is navigated around a blood vessel with sequential steps sampling from a spiral pattern. Blood vessel in A and B shown in isometric view. Blood vessel in C shown in top view (top) and cross section (bottom).

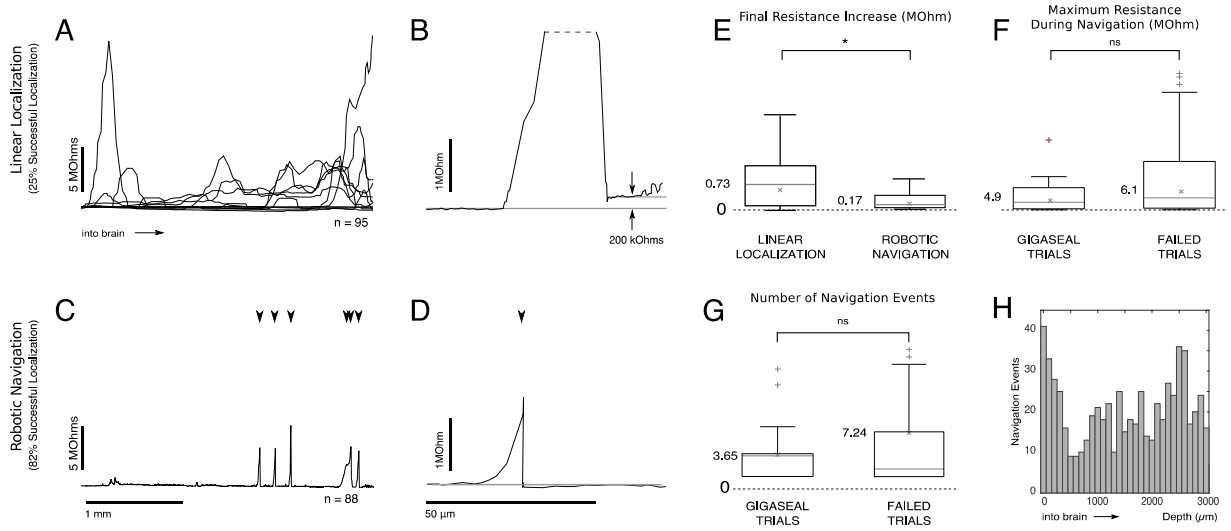

Figure 4: Pipette tip resistance increases during regional pipette localization in vivo due to accrued debris, preventing whole cell recordings. Robotic navigation prevents this debris from accruing. A) Recordings of change in pipette resistance during regional pipette localization reveal that obstructions are encountered throughout the insertion path. B) When an obstruction is cleared by continuing linear pipette advancement, debris may still be present at the pipette tip, reflected by the persistent resistance increase of the pipette by 200kOhms. C) Using a robotic navigation algorithm, pipette debris is prevented from accruing on the pipette tip, shown by the return of the pipette resistance to the baseline. Arrows indicate locations of robotic navigation event. D) Detail of a single robotic navigation event. A-D) initial pipette resistance was subtracted to show changes in resistance. Initial pipette resistances ranged from 4-7 MΩ. E) The final resistance of the pipette is significantly lower after insertion to 3mm below the pial surface when the robotic navigation algorithm to localize the pipette was used. F) The maximum resistance measured during robotic navigation is not significantly different between trials that gigasealed successfully (n=17) and trials that failed to seal (n=71), Wilcoxon rank sum test (p=0.19). G) The number of navigation events was not significantly different between trials that gigasealed successfully (n=17) and trials that failed to seal (n=71), Wilcoxon rank sum test (p=0.96) H) Histogram showing number of navigation events as a function of depth. Note the slight increase in navigation events around 0 µm and 2500 µm from the pial surface, where the pia and ventricular meninges were encountered, respectively.

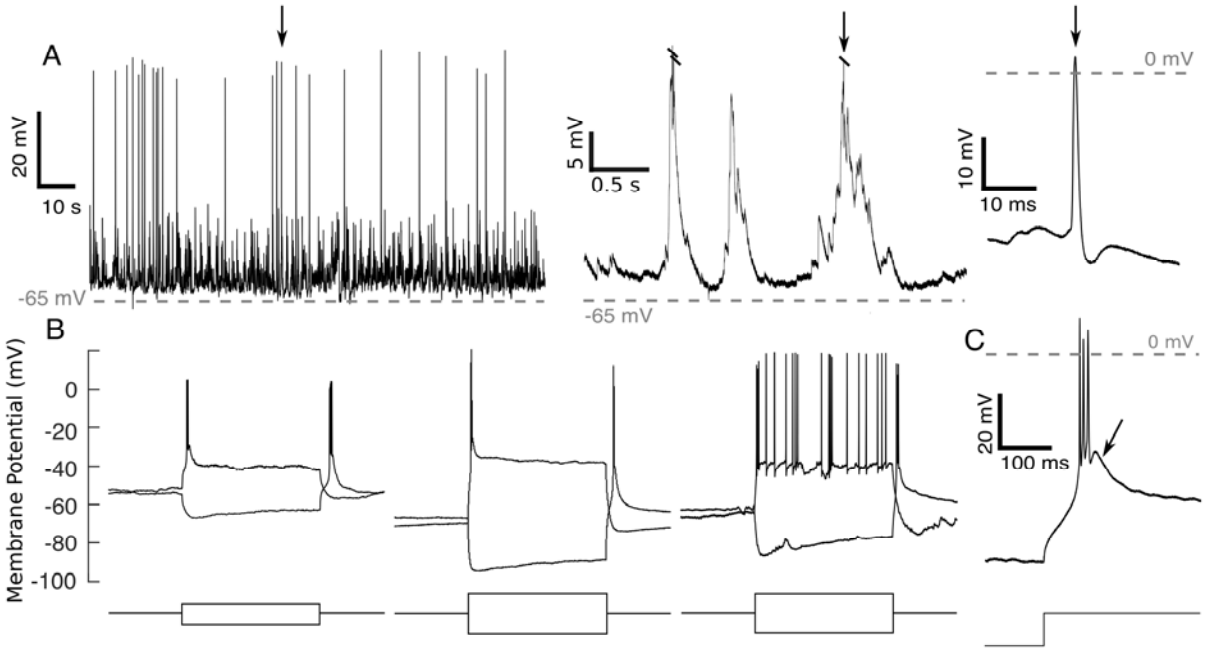

Figure 5: Neurons recorded in whole-cell configuration were of good quality. A) Example of spontaneous activity from a neuron recorded 3.2 mm below the pial surface with detail of spontaneous burst (arrow indicates burst shown in detail to the right). B) Example whole-cell traces recorded in the thalamus for 3 different neurons. Note the sag in membrane potential following hyperpolarizing current injection (representing activity of $I_{h,}$(Leist et al., 2016)) and after-hyperpolarization rebound bursting in each trace, indicative of thalamic neurons. Current injections lasted 0.5 sec and ranged from ± 50 pA (first recording) to ± 100 pA (second and third recording). C) Following hyperpolarizing current injection, rebound bursts exhibited after depolarization (ADP, see arrow, (X. Wang et al., 2010b)), consistent with ventrobasal thalamic nucleus cells. Current injection was -150 pA.

REFERENCES

Arkhipov, A., Berg, J., Buice, M., Gouwens, N. W., Gratiy, S., Iyer, R., et al. (2016). Inferring cortical function in the mouse visual system through large-scale systems neuroscience. *Proceedings of the National Academy of Sciences*, *113*(27), 7337–7344. http://doi.org/10.1073/pnas.1512901113

Bargmann, C., Newsome, W., & Anderson, A. (2014). BRAIN 2025: a scientific vision. *… /Science/Brain/2025/(….*

Benavides, D. R., Quinn, J. J., Zhong, P., Hawasli, A. H., DiLeone, R. J., Kansy, J. W., et al. (2007). Cdk5 modulates cocaine reward, motivation, and striatal neuron excitability. *The Journal of Neuroscience : the Official Journal of the Society for Neuroscience*, *27*(47), 12967–12976. http://doi.org/10.1523/JNEUROSCI.4061-07.2007

Blanton, M. G., Loturco, J. J., & Kriegstein, A. R. (1989). Whole Cell Recording From Neurons in Slices of Reptilian and Mammalian Cerebral-Cortex. *Journal of Neuroscience Methods*, *30*(3), 203–210.

Brecht, M., & Sakmann, B. (2002). Whisker maps of neuronal subclasses of the rat ventral posterior medial thalamus, identified by whole-cell voltage recording and morphological reconstruction. *The Journal of Physiology*, *538*(2), 495–515. http://doi.org/10.1113/jphysiol.2001.012334

Cadwell, C. R., Palasantza, A., Jiang, X., Berens, P., Deng, Q., Yilmaz, M., et al. (2016). Electrophysiological, transcriptomic and morphologic profiling of single neurons using Patch-seq. *Nature Biotechnology*, *34*(2), 199–203. http://doi.org/10.1038/nbt.3445

Constantinople, C. M., & Bruno, R. M. (2013). Deep Cortical Layers Are Activated Directly by Thalamus. *Science*, *340*(6140), 1591–1594. http://doi.org/10.1126/science.1236425

Desai, N. S., Siegel, J. J., Taylor, W., Chitwood, R. A., & Johnston, D. (2015). MATLAB-based automated patch-clamp system for awake behaving mice. *Journal of Neurophysiology*, *114*(2), 1331–1345. http://doi.org/10.1152/jn.00025.2015

Fee, M. S. (2000). Active stabilization of electrodes for intracellular recording in awake behaving animals. *Neuron*, *27*(3), 461–468.

Friedberg, M. H., Lee, S. M., & Ebner, F. F. (2004). The contribution of the principal and spinal trigeminal nuclei to the receptive field properties of thalamic VPM neurons in the rat. *Journal of Neurocytology*, *33*(1), 75–85. http://doi.org/10.1023/B:NEUR.0000029649.28599.a5

Groh, A., Bokor, H., Mease, R. A., Plattner, V. M., Hangya, B., Stroh, A., et al. (2014). Convergence of cortical and sensory driver inputs on single thalamocortical cells. *Cerebral Cortex*, *24*(12), 3167–3179. http://doi.org/10.1093/cercor/bht173

Guo, M.-L., Xue, B., Jin, D.-Z., Liu, Z.-G., Fibuch, E. E., Mao, L.-M., & Wang, J. Q. (2012). Upregulation of Npas4 protein expression by chronic administration of amphetamine in rat nucleus accumbens in vivo. *Neuroscience Letters*, *528*(2), 210–214. http://doi.org/10.1016/j.neulet.2012.07.048

Harvey, C. D., Collman, F., Dombeck, D. A., & Tank, D. W. (2009). Intracellular dynamics of hippocampal place cells during virtual navigation. *Nature*, *461*(7266), 941–946. http://doi.org/10.1038/nature08499

Higley, M. J., & Contreras, D. (2007). Cellular Mechanisms of Suppressive Interactions Between Somatosensory Responses In Vivo. *Journal of Neurophysiology*, *97*(1), 647–658. http://doi.org/10.1152/jn.00777.2006

Hu, X.-T., Nasif, F. J., Zhang, J., & Xu, M. (2008). Fos regulates neuronal activity in the nucleus accumbens. *Neuroscience Letters*, *448*(1), 157–160. http://doi.org/10.1016/j.neulet.2008.10.025

Kase, D., Inoue, T., & Imoto, K. (2012). Roles of the subthalamic nucleus and subthalamic HCN channels in absence seizures. *Journal of Neurophysiology*, *107*(1), 393–406. http://doi.org/10.1152/jn.00937.2010

Kelly, S. T., Kremkow, J., Jin, J., Wang, Y., Wang, Q., Alonso, J.-M., & Stanley, G. B. (2014). The Role of Thalamic Population Synchrony in the Emergence of Cortical Feature Selectivity. *PLOS Comput Biol*, *10*(1), e1003418. http://doi.org/10.1371/journal.pcbi.1003418

Kodandaramaiah, S. B., Franzesi, G. T., Chow, B. Y., Boyden, E. S., & Forest, C. R. (2012). Automated whole-cell patch-clamp electrophysiology of neurons in vivo. *Nature Methods*, *9*(6), 585–587. http://doi.org/10.1038/nmeth.1993

699 Kodandaramaiah, S. B., Holst, G. L., Wickersham, I. R., Singer, A. C., Franzesi, G. T., McKinnon, M. L.,
700 et al. (2016). Assembly and operation of the autopatcher for automated intracellular neural recording
701 in vivo. *Nature Protocols*, *11*(4), 634–654. http://doi.org/10.1038/nprot.2016.007
702 Kolb, I., Stoy, W. A., Rousseau, E. B., Moody, O. A., Jenkins, A., & Forest, C. R. (2016). Cleaning patch-
703 clamp pipettes for immediate reuse. *Scientific Reports*, *6*. http://doi.org/10.1038/srep35001
704 Kuisle, M., Wanaverbecq, N., Brewster, A. L., Frère, S. G. A., Pinault, D., Baram, T. Z., & Lüthi, A. (2006).
705 Functional stabilization of weakened thalamic pacemaker channel regulation in rat absence epilepsy.
706 *The Journal of Physiology*, *575*(1), 83–100. http://doi.org/10.1113/jphysiol.2006.110486
707 Kuo, R. I., & Wu, G. K. (2012). The Generation of Direction Selectivity in the Auditory System. *Neuron*,
708 *73*(5), 1016–1027. http://doi.org/10.1016/j.neuron.2011.11.035
709 Lee, A. K., Epsztein, J. E. R. O. M., & Brecht, M. (2009). Head-anchored whole-cell recordings in freely
710 moving rats. *Nature Protocols*, *4*(3), 385–392. http://doi.org/10.1038/nprot.2009.5
711 Lee, D., Shtengel, G., Osborne, J. E., & Lee, A. K. (2014). Anesthetized- and awake-patched whole-cell
712 recordings in freely moving rats using UV-cured collar-based electrode stabilization. *Nature*
713 *Protocols*, *9*(12), 2784–2795. http://doi.org/10.1038/nprot.2014.190
714 Leist, M., Datunashvilli, M., Kanyshkova, T., Zobeiri, M., Aissaoui, A., Cerina, M., et al. (2016). Two types
715 of interneurons in the mouse lateral geniculate nucleus are characterized by different h-current
716 density. *Scientific Reports*, *6*, 24904. http://doi.org/10.1038/srep24904
717 Lin, M. Z., & Schnitzer, M. J. (2016). Genetically encoded indicators of neuronal activity. *Nature*
718 *Neuroscience*, *19*(9), 1142–1153. http://doi.org/10.1038/nn.4359
719 Llinás, R. R., & Steriade, M. (2006). Bursting of Thalamic Neurons and States of Vigilance. *Journal of*
720 *Neurophysiology*, *95*(6), 3297–3308. http://doi.org/10.1152/jn.00166.2006
721 Margrie, T. W., Brecht, M., & Sakmann, B. (2002). In vivo, low-resistance, whole-cell recordings from
722 neurons in the anaesthetized and awake mammalian brain. *Pflügers Archiv*, *444*(4), 491–498.
723 http://doi.org/10.1007/s00424-002-0831-z
724 Margrie, T. W., Meyer, A. H., Caputi, A., Monyer, H., Hasan, M. T., Schaefer, A. T., et al. (2003). Targeted
725 Whole-Cell Recordings in the Mammalian Brain In Vivo. *Neuron*, *39*(6), 911–918.
726 http://doi.org/10.1016/j.neuron.2003.08.012
727 Mease, R. A., Sumser, A., Sakmann, B., & Groh, A. (2016). Cortical Dependence of Whisker Responses
728 in Posterior Medial Thalamus In Vivo. *Cerebral Cortex*, *26*(8), bhw144–3543.
729 http://doi.org/10.1093/cercor/bhw144
730 Neher, E. (1995). … , ION CHANNELS FOR COMMUNICATION BETWEEN AND WITHIN CELLS,
731 DECEMBER 9, 1991 BY ERWIN NEHER AND ELEMENTARY STEPS IN …. Nobel Lectures.
732 Neuhoff, H., Neu, A., Liss, B., & Roeper, J. (2002). I(h) channels contribute to the different functional
733 properties of identified dopaminergic subpopulations in the midbrain. *The Journal of Neuroscience :*
734 *the Official Journal of the Society for Neuroscience*, *22*(4), 1290–1302.
735 Oberlaender, M., de Kock, C. P. J., Bruno, R. M., Ramirez, A., Meyer, H. S., Dercksen, V. J., et al.
736 (2012a). Cell type-specific three-dimensional structure of thalamocortical circuits in a column of rat
737 vibrissal cortex. *Cerebral Cortex*, *22*(10), 2375–2391. http://doi.org/10.1093/cercor/bhr317
738 Oberlaender, M., Ramirez, A., & Bruno, R. M. (2012b). Sensory experience restructures thalamocortical
739 axons during adulthood. *Neuron*, *74*(4), 648–655. http://doi.org/10.1016/j.neuron.2012.03.022
740 Petersen, R. S., Brambilla, M., Bale, M. R., Alenda, A., Panzeri, S., Montemurro, M. A., & Maravall, M.
741 (2008). Diverse and temporally precise kinetic feature selectivity in the VPm thalamic nucleus.
742 *Neuron*, *60*(5), 890–903. http://doi.org/10.1016/j.neuron.2008.09.041
743 Polack, P. O., & Charpier, S. (2006). Intracellular activity of cortical and thalamic neurones during
744 high-voltage rhythmic spike discharge in Long-Evans rats in vivo. *The Journal of Physiology*, *571*(2),
745 461–476. http://doi.org/10.1113/jphysiol.2005.100925
746 Porcello, D. M., Ho, C. S., Joho, R. H., & Huguenard, J. R. (2002). Resilient RTN fast spiking in Kv3.1 null
747 mice suggests redundancy in the action potential repolarization mechanism. *Journal of*
748 *Neurophysiology*, *87*(3), 1303–1310.
749 Rancz, E. A., Franks, K. M., Schwarz, M. K., Pichler, B., Schaefer, A. T., & Margrie, T. W. (2011).
750 Transfection via whole-cell recording in vivo: bridging single-cell physiology, genetics and
751 connectomics. *Nature Neuroscience*, *14*(4), 527–532. http://doi.org/10.1038/nn.2765
752 Santisakultarm, T. P., Cornelius, N. R., Nishimura, N., Schafer, A. I., Silver, R. T., Doerschuk, P. C., et al.
753 (2012). In vivo two-photon excited fluorescence microscopy reveals cardiac- and respiration-
754 dependent pulsatile blood flow in cortical blood vessels in mice. *American Journal of Physiology-*

Heart and Circulatory Physiology, *302*(7), H1367–H1377. http://doi.org/10.1152/ajpheart.00417.2011
Sánchez, D., Johnson, N., Li, C., Novak, P., Rheinlaender, J., Zhang, Y., et al. (2008). Noncontact Measurement of the Local Mechanical Properties of Living Cells Using Pressure Applied via a Pipette. *Biophysical Journal*, *95*(6), 3017–3027. http://doi.org/10.1529/biophysj.108.129551
Sherman, S. M. (2005). The role of the thalamus in cortical function: not just a simple relay.
Singh, A., Zhu, H., & He, J. (2004). Improving mechanical stiffness of coated benzocyclobutene (BCB) based neural implant. *Conference Proceedings : ... Annual International Conference of the IEEE Engineering in Medicine and Biology Society. IEEE Engineering in Medicine and Biology Society. Annual Conference*, *6*, 4298–4301. http://doi.org/10.1109/IEMBS.2004.1404197
Sosulina, L., Graebenitz, S., & Pape, H.-C. (2010). GABAergic interneurons in the mouse lateral amygdala: a classification study. *Journal of Neurophysiology*, *104*(2), 617–626. http://doi.org/10.1152/jn.00207.2010
Stuart, G. J., Dodt, H. U., & Sakmann, B. (1993). Patch-clamp recordings from the soma and dendrites of neurons in brain slices using infrared video microscopy. *Pflügers Archiv*, *423*(5-6), 511–518. http://doi.org/10.1007/BF00374949
Vélez-Fort, M., Rousseau, C. V., Niedworok, C. J., Wickersham, I. R., Rancz, E. A., Brown, A. P. Y., et al. (2014). The Stimulus Selectivity and Connectivity of Layer Six Principal Cells Reveals Cortical Microcircuits Underlying Visual Processing. *Neuron*, *83*(6), 1431–1443. http://doi.org/10.1016/j.neuron.2014.08.001
Wang, Q., Webber, R. M., & Stanley, G. B. (2010a). Thalamic synchrony and the adaptive gating of information flow to cortex. *Nature Neuroscience*, *13*(12), 1534–1541. http://doi.org/10.1038/nn.2670
Wang, X., Vaingankar, V., Sanchez, C. S., Sommer, F. T., & Hirsch, J. A. (2011). Thalamic interneurons and relay cells use complementary synaptic mechanisms for visual processing. *Nature Neuroscience*, *14*(2), 224–231. http://doi.org/10.1038/nn.2707
Wang, X., Wei, Y., Vaingankar, V., Wang, Q., Koepsell, K., Sommer, F. T., & Hirsch, J. A. (2007). Feedforward excitation and inhibition evoke dual modes of firing in the cat's visual thalamus during naturalistic viewing. *Neuron*, *55*(3), 465–478. http://doi.org/10.1016/j.neuron.2007.06.039
Wang, X., Yu, G., Hou, X., Zhou, J., Yang, B., & Zhang, L. (2010b). Rebound bursts in GABAergic neurons of the thalamic reticular nucleus in postnatal mice.
Wu 吴秋雨, Q., Kolb, I., Callahan, B. M., Su, Z., Stoy, W., Kodandaramaiah, S. B., et al. (2016). Integration of autopatching with automated pipette and cell detection in vitro. *Journal of Neurophysiology*, *116*(4), 1564–1578. http://doi.org/10.1152/jn.00386.2016
Yu, Y.-Q., Xiong, Y., Chan, Y.-S., & He, J. (2004a). Corticofugal Gating of Auditory Information in the Thalamus: An In Vivo Intracellular Recording Study. *Journal of Neuroscience*, *24*(12), 3060–3069. http://doi.org/10.1523/JNEUROSCI.4897-03.2004
Yu, Y.-Q., Xiong, Y., Chan, Y.-S., & He, J. (2004b). Corticofugal gating of auditory information in the thalamus: an in vivo intracellular recording study. *The Journal of Neuroscience : the Official Journal of the Society for Neuroscience*, *24*(12), 3060–3069. http://doi.org/10.1523/JNEUROSCI.4897-03.2004

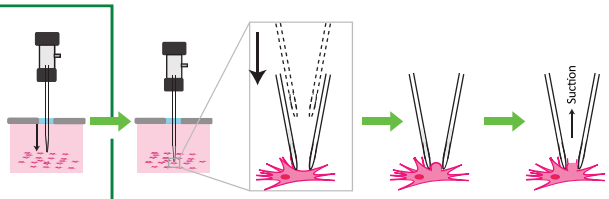

Region	Depth	RPL Method	Regional Pipette Localization **(RPL)**	Neuron Hunting	Gigaseal Formation	Break In	Total Yield
Cortex	≤ 1 mm	Linear	81%	93%	51%	82%	31%
Thalamus	≥ 3 mm	Linear	25%	88%	10%	50%	1%
		n=	24/95	21/24	2/21	1/2	1/95
Thalamus	≥ 3 mm	Robotic	82%	89%	26%	53%	10%
		n=	72/88	64/72	17/64	9/17	9/88

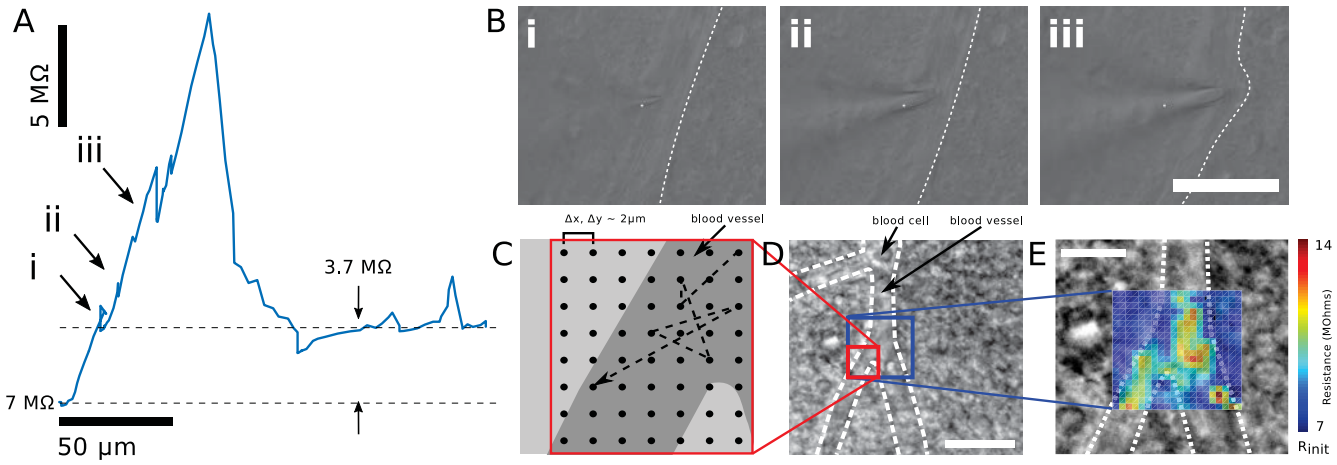
A
5 MΩ
iii
ii
i
3.7 MΩ
7 MΩ
50 µm
B
i
ii
iii
C
Δx, Δy ~ 2µm
blood vessel
D
blood cell
blood vessel
E
14
Resistance (MOhms)
7
Rinit

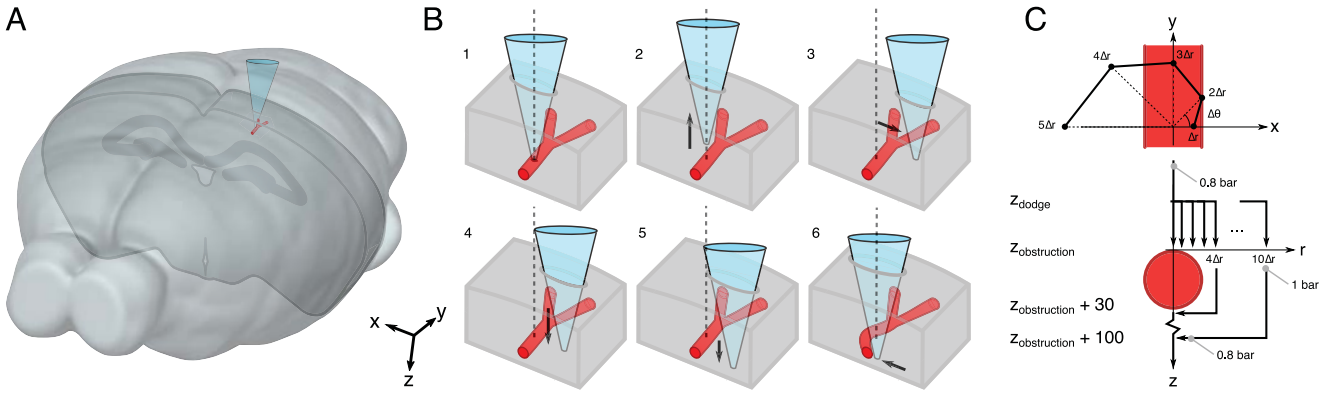
A
B
C
1
2
3
4
5
6
x
y
z
y
4Δr
3Δr
2Δr
Δθ
Δr
5Δr
x
0.8 bar
z_dodge
z_obstruction
4Δr
10Δr
r
1 bar
z_obstruction + 30
z_obstruction + 100
0.8 bar
z

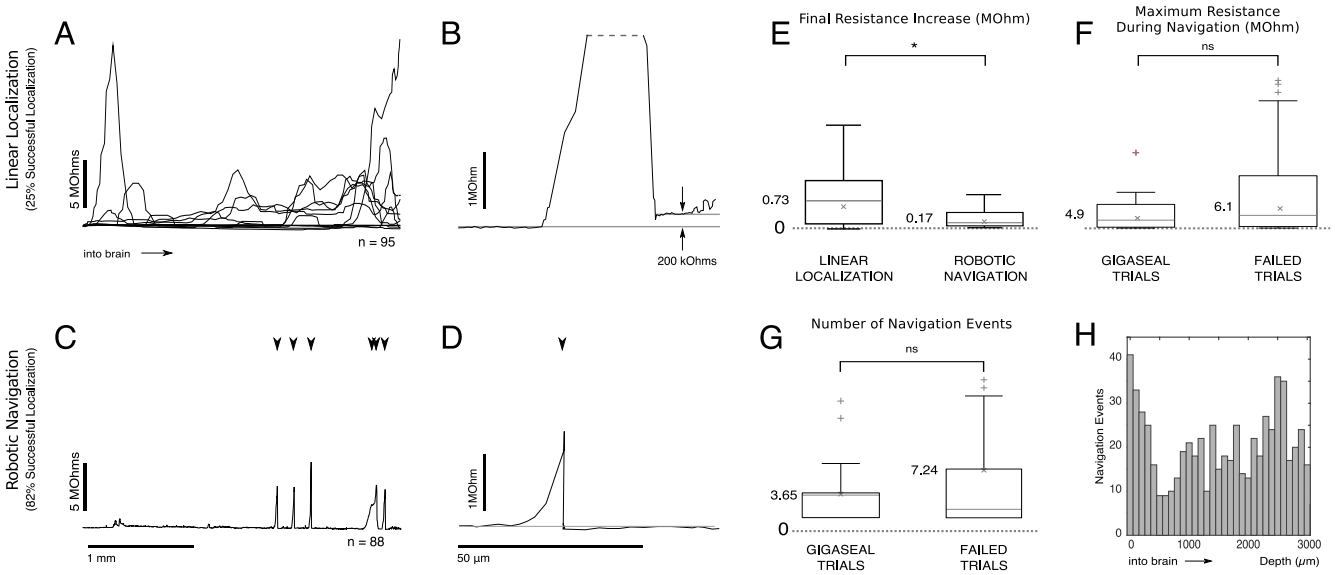
A
Linear Localization
(25% Successful Localization)
5 MOhms
into brain
n = 95
B
1MOhm
200 kOhms
E
Final Resistance Increase (MOhm)
*
0.73
0
0.17
LINEAR LOCALIZATION
ROBOTIC NAVIGATION
F
Maximum Resistance During Navigation (MOhm)
ns
4.9
6.1
GIGASEAL TRIALS
FAILED TRIALS
C
Robotic Navigation
(82% Successful Localization)
5 MOhms
1 mm
n = 88
D
1MOhm
50 µm
G
Number of Navigation Events
ns
3.65
0
7.24
GIGASEAL TRIALS
FAILED TRIALS
H
Navigation Events
40
30
20
10
0
0
1000
2000
3000
into brain
Depth (µm)

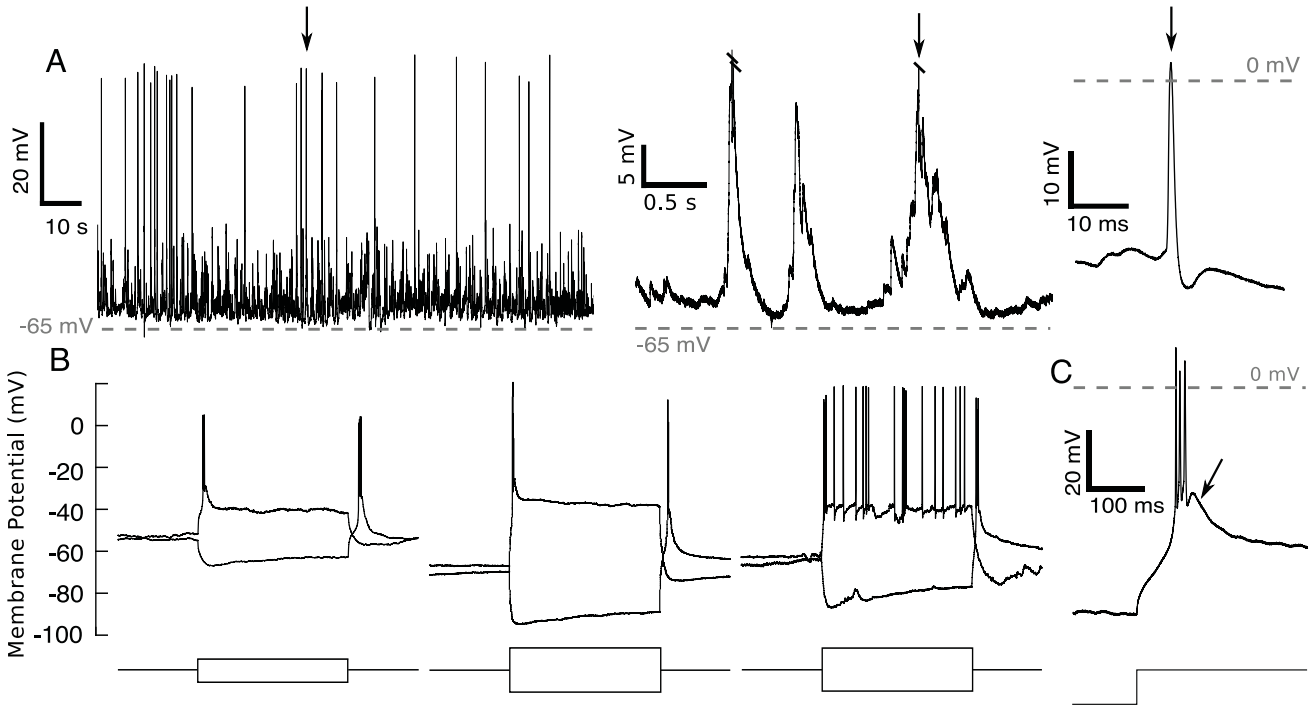
A
20 mV
10 s
-65 mV
5 mV
0.5 s
-65 mV
0 mV
10 mV
10 ms
B
Membrane Potential (mV)
0
-20
-40
-60
-80
-100
C
0 mV
20 mV
100 ms